

ShoeRinsics: Shoeprint Prediction for Forensics with Intrinsic Decomposition

Samia Shafique¹, Bailey Kong¹, Shu Kong², and Charless C. Fowlkes¹

¹ Dept. of Computer Science, University of California, Irvine

² Robotics Institute, Carnegie Mellon University

{sshafiqu, bhkong, fowlkes}@ics.uci.edu, shuk@andrew.cmu.edu

<https://github.com/Samia067/ShoeRinsics>

Abstract. Shoe tread impressions are one of the most common types of evidence left at crime scenes. However, the utility of such evidence is limited by the lack of databases of footwear impression patterns that cover the huge and growing number of distinct shoe models. We propose to address this gap by leveraging shoe tread photographs collected by online retailers. The core challenge is to predict the impression pattern from the shoe photograph since ground-truth impressions or 3D shapes of tread patterns are not available. We develop a model that performs intrinsic image decomposition (predicting depth, normal, albedo, and lighting) from a single tread photo. Our approach, which we term *ShoeRinsics*, combines domain adaptation and re-rendering losses in order to leverage a mix of fully supervised synthetic data and unsupervised retail image data. To validate model performance, we also collected a set of paired shoe-sole images and corresponding prints, and define a benchmarking protocol to quantify the accuracy of predicted impressions. On this benchmark, ShoeRinsics outperforms existing methods for depth prediction and synthetic-to-real domain adaptation.

Keywords: Shoeprints · Forensic Evidence · Depth Prediction · Intrinsic Decomposition · Domain Adaptation

1 Introduction

Studying the evidence left at a crime scene aids investigators in identifying criminals. Although shoeprints may have fewer uniquely identifying characteristics than other biometric samples (such as blood or hair), they have a greater chance of being present at crime scenes [11]. Thus, the study of shoeprints can provide valuable clues to help investigators narrow down suspects of a crime.

Forensic analysis of shoeprints can provide clues on the *class characteristics* as well as the *acquired characteristics* of the suspect’s shoe. Class characteristics involve the type of shoe (such as the brand, model, and size) whereas the acquired characteristics consist of the individual characteristics of a particular shoe as it is worn over time (such as holes, cuts, and scratches). We are interested in aiding the study of class characteristics of shoeprints.

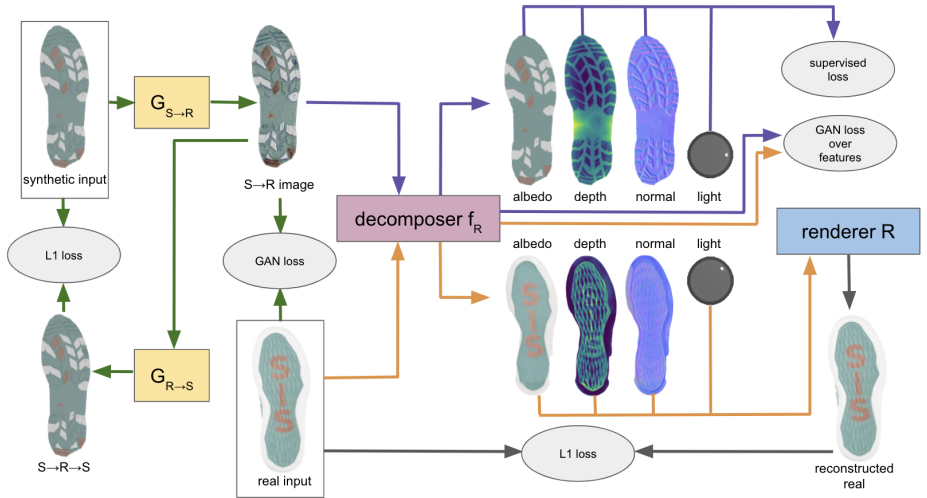


Fig. 1. The flowchart of our method *ShoeRinsics* in training. The training data consists of synthetic images labeled with intrinsic components and unlabeled real images. Conceptually, *ShoeRinsics* incorporates intrinsic decomposition (right part) and domain adaptation (left part) to learn a depth predictor for real shoe-sole images. We use a renderer pre-trained on synthetic data to regularize intrinsic decomposition from which we obtain depth predictions. We find this works better than learning to predict depth only, presumably because intrinsic decomposition leverages extra supervision from synthetic data that helps depth prediction learning.

Traditionally, investigating class characteristics of shoeprints involves matching the prints against a manually curated database of impressions of various different shoe models [2]. There has been significant interest in the research community in automating this querying process [12,13,22,23,24,5,30,33,32,57,65]. However, the success of such work in real life depends largely on the quality of the database to which the shoeprint evidence is compared. If the database does not include the type of shoe the criminal wore, then such methods would not prove useful. Unfortunately, maintaining and regularly updating a database to include all types of shoes is tedious, costly, and requires significant human effort. It is also partly because of this lack of a reference database that shoeprint evidence is vastly underutilized in the USA.

To address this gap, we propose to leverage imagery of shoe treads that are collected by online retailers. High-resolution photos of treads associated with shoe products are readily available and shopping websites are updated frequently (based on monitoring a few sites we estimate 1000s of new products appear each month). Examples of such shoe tread images are shown in Figure 2 (b). The primary technical challenge is to estimate the contact surface (*shoeprint*) or more generally, the 3D shape of the tread from a single tread photograph. Developing automated models for predicting prints from tread images would directly address the need for a comprehensive, up-to-date database of tread patterns.

To learn to predict the 3D shape of shoe treads from single images, we would ideally utilize supervised training examples of aligned shoe tread images and their corresponding depth maps. However, since such ground-truth data simply isn't available we developed an alternate strategy. Instead, we created a synthetic dataset of rendered shoe-sole images and corresponding aligned ground-truth albedo, depth, normal images, and lighting configuration. This data can be used to train a predictor in a fully supervised fashion but the resulting model performs sub-optimally on real-world images due to domain shift between synthetic and real imagery. To address this, we introduce three additional training criteria which leverage real-world images (see Figure 1). First, we utilize a cycle-GAN based domain "translator" that adjusts synthetic data to better match the distribution of the real shoe images, i.e., low-level domain adaptation. Second, we introduce an adversarial loss that enforces that decomposer features are similar across real and synthetic images, i.e., high-level domain adaptation. Finally, we re-render the predicted tread depth/albedo/lighting and require that the result matches the real input image. The combination of both high-level and low-level domain adaptation with self-supervised reconstruction yields superior adaptation to real tread photos.

Motivated to address the need for an automated and comprehensive footwear impression database, we make three major contributions as below.

- We introduce the problem of shoeprint prediction from tread photos, curate datasets, and set up an evaluation protocol for benchmarking predictions.
- We tailor existing methods for depth prediction and domain adaptation to the task of shoeprint prediction and analyze their merits.
- We show that by incorporating both intrinsic decomposition and domain adaptation techniques, our method *ShoeRinsics* outperforms existing methods in predicting impressions from tread photos.

2 Related Work

Shoeprint Analysis. Automatic shoeprint matching has been studied widely in the past two decades [45]. State-of-the-art work has focused on generating good features from shoeprints and using them to assign a class label (shoe type) from a database of lab footwear impressions. To study the global features of shoeprints (i.e., considering the whole shoe) [33] introduces a probabilistic compositional active basis model, [32] explores multi-channel normalized cross-correlation to match multi-channel deep features, [57] employs a manifold ranking method and [65] uses VGG16 as a feature extractor. On the other hand, [41] studies a multi-part weighted CNN, [7] introduces the blocking sparse representation technique, [8] applies multiple point-of-interest detectors and SIFT descriptors to study the local features of shoeprints (i.e., keypoints [34]). Our work differs from previous methods as it focuses on automatically generating the query database instead of automatically matching a query shoeprint to a specific reference impression in the database.

Depth Prediction. Monocular depth estimation has been studied extensively since early works [27,48,47]. Literature in this domain utilize handcrafted representations [10,44,19], DCNNs [9,37,46,31,36,60], and sophisticated training losses [17,51,61]. [35,21,38] explore self-supervised learning in a stereo setup while [43,67] experiment with training on large datasets. Depth estimation has been further improved by considering the camera pose in [66]. Our work differs from classic monocular depth estimation by learning depth in a semi-supervised way while using only single images during training and imposing structure using intrinsic image decomposition.

Intrinsic Image Decomposition. Another line of work proposes to explain image appearance in terms of decomposition into a set of intrinsic images - albedo and shading, or further into normals, and lighting. However, determining ground-truth intrinsic images is difficult if not impossible in the wild. Our approach is related to [29] which decomposes images to intrinsic components and then uses a differentiable renderer to reconstruct input images in order to leverage unlabeled data. [50,42,58] focus explicitly on face decompositions. [50] proposes a similar reconstruction loop while [42] explicitly models non-diffuse lighting. [58] discusses a way to incorporate multiple reflectance channels to model faces. [59] works on rotationally symmetric objects to learn intrinsic decomposition from real data with only the silhouette of the object as supervision. [49,63,69,39,62] study decomposition on entire scenes. Adversarial networks have only recently been used for intrinsic image decomposition. [6] takes unpaired data as input to learn photo-realistic rendering of synthetic data and intrinsic decomposition of real images using an adversarial loss. Another direction that has been explored recently uses a sequence of images as input [64,52]; however, we aim to learn from only single training images. We find that learning with intrinsic decomposition on synthetic images alone can produce sub-optimal results on real images. Thus, our work performs image space and feature space alignment between the two domains in addition to performing intrinsic image decomposition.

Domain Adaptation. Training solely on synthetic data can cause models to perform poorly on real data. Adversarial domain adaptation has proved promising for bridging such domain gaps. One way to approach this is to use domain invariant features to map between the domains. [40] proposes a Transfer Component Analysis method to reduce the Maximum Mean Discrepancy to learn domain invariant features. [56] builds on this idea and further improves domain adaptation performance in classification tasks. [55,54,20,53] learn domain adaptation by aligning source and target features. Another direction of work uses image-to-image translation [70] to stylize source images as target images. [26] and [68] use the stylized source images to learn from target images using source labels while performing alignment both at an image level and at the feature level. We use domain adaptation for the problem of depth estimation but take this approach further by reasoning about the intrinsic components of unlabeled real data.

Table 1. Overview of our datasets for training, validation, and testing. We further list shoe categories in the datasets and their counts. It is worth noting that Real-val contains formal and used shoes which are not included in the training sets. We include these new shoe types in validation to study if our method still works on never-before-seen shoe types. Please refer to Figure 2 for visual examples.

Dataset	Shoe Category			Total	Annotation
	New, Athletic	Formal	Used		
Syn-train	88,408	0	0	88,408	depth, albedo, normal, light
Real-train	3,543	0	0	3,543	none
Real-test	269	0	0	269	none
Real-val	22	6	8	36	print



Fig. 2. Shoe-sole examples from Syn-train (a), Real-train (b), and Real-val (c). It is clear that there exists a domain gap between synthetic (a) and real shoes (b), demonstrating the need to close the synthetic-to-real domain gap. Moreover, Real-val contains formal and used shoes which are not present during training. We use them to study how methods perform on these never-before-seen images.

3 Dataset Construction and Problem Setup

We propose three new shoe-sole datasets to train and validate our model. An overview of the datasets is provided in Table 1 and sample shoe-soles are shown in Figure 2. We train on Syn-train (synthetic images with ground-truth intrinsic labels) and Real-train (real images without ground-truth) and evaluate on Real-val (real images with ground-truth prints). Our training datasets only contain new athletic shoes while our evaluation dataset also contains some formal and used shoes. This provides a way to check the robustness of our method compared to others.

3.1 Synthetic Shoe Dataset (Syn-train)

To train our model, we need shoe-sole images with paired ground-truth albedo, depth, normal and light information. Publicly available datasets that include shoe objects (among other categories) [4] either do not focus on the shoe-sole and/or do not provide full decomposition into shape, albedo, and lighting. Thus, we introduce our own synthetic dataset, Syn-train. For this purpose, we first create plausible depth maps, albedo maps, and lighting environments (outlined in Figure 3). We pass these to a rendering engine to generate synthetic images along with paired ground-truth albedo, depth, normal, and light. We observe

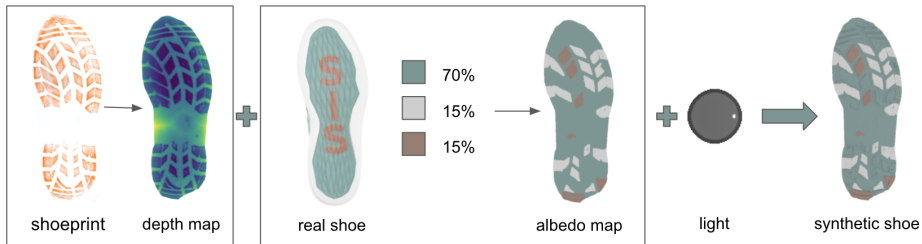


Fig. 3. Generation of synthetic data. A shoeprint is used to generate a hypothetical depth map. This depth map and a color distribution obtained from a real-shoe example is used to create an albedo map. The depth map and albedo map are combined with a light environment to render a synthetic shoe-sole image. The light environment is demonstrated by visualizing a shiny sphere in the place of the shoe. In this example, directional light is coming from a point on the right.

that commercial shoe tread photographs are taken under very diffuse lighting conditions where the primary variations in surface brightness are driven by global illumination effects rather than surface normal orientation (e.g., grooves appear darker). This necessitates the use of a physically-based rendering engine [28] rather than simple local shading models often used previously in intrinsic image decomposition. Our final synthetic dataset contains a total of 88,408 shoe-sole images with paired ground-truth intrinsics.

Depth Map. We start with some images of shoeprints collected in a controlled lab environment. We convert the 2D shoeprints to 3D depth maps by adding hypothetical heights to each point on the print. Each print is further randomized in multiple slightly different ways to create a variety of depth maps. First, we extract the low-frequency component of the print which corresponds to the larger tread elements of the shoe. Then, we add some moderate amount of high-frequency details to the depth map. We optionally add other features which are common in real shoes (such as adding slanted bevels to the tread elements and curving up the sides of the shoes slightly) to make the depth maps look more realistic. We use a total of 339 different shoeprints and produce 10-15 different depth maps from each of those prints.

Albedo Map. The color palette for each of the rendered shoes comes from the color distribution of a real shoe-sole photograph. Shoes tend to have only a handful of different colors across the entire sole. We identify the main colors on real shoe-soles using the mean-shift algorithm [18]. These colors are used to create albedo maps for the rendered shoes. First, we use depth maps to identify shoe-tread elements and segment out areas of the shoe that can have different colors. Then we assign colors to those segments from the color palette of a real shoe in the percentages in which they are present. One example is shown in Figure 3.

Light environment. Online retail stores photograph shoes using specialized diffuse lighting rigs. We create a similar light environment for our rendered images. Shoes are photographed with bright diffuse white light from all directions and some optional directional light. We use a total of 17 different light configu-

rations in Syn-train. One light configuration is simply diffuse light coming from all directions. Eight light configurations consist of single light bulbs shining from the eight directions around the shoe in addition to the diffuse white light. The other eight light configurations are similar but consist of two light bulbs at 120° to each other.

3.2 Unlabeled Real Shoe Dataset (Real-train and Real-test)

Shoes sold by online retailers [1,3] are advertised using photos of the shoes which include shoe-sole images. We collect such shoe-sole images and add masks computed by a simple network to segment out the shoe-soles. This dataset does not contain any ground-truth and consists only of new, athletic shoes. We split this dataset into Real-train (3,543) and Real-test (269).

3.3 Labeled Real Shoe Dataset (Real-val)

To test our method, we collect shoe-sole image and print pairs of real shoes. We photograph shoes by placing them inside a light box with a ring light on top. We also collect prints from those shoes by painting the soles of the shoes with a thin layer of relief ink and pressing an absorbent white paper onto the soles of the shoes. This method of collecting shoeprints is called the *block printing technique* and is one of several techniques used in the forensics community to collect reference footwear impressions (detailed in the appendix). To improve print quality, we collect 2-3 sets of prints for each shoe and use the average print after aligning them to the shoe-tread photograph. The average prints are then aligned to the shoe-sole image. We use thin plate splines [14] with a smoothness parameter of 0.5 for alignment. The final shoeprint is binary and determined by thresholding the aligned print.

Real-val contains 22 new athletic shoes, 6 new formal shoes, and 8 used athletic shoes. While new athletic shoes are present in our training dataset, formal and used shoes are not.

3.4 Problem Setup

Given Syn-train and Real-train, we aim to correctly predict depth from Real-test and Real-val. Syn-train contains synthetic shoe-sole images and paired ground-truth decompositions while Real-train consists of unlabeled real shoe-sole images. Real-val contains shoe-sole images and ground-truth print which is used for evaluation. We threshold the depth prediction on Real-val to obtain shoeprint predictions as described in Section 3.5. We further do qualitative analysis on Real-test which contains unlabeled real shoes.

3.5 Evaluation Metric

Given the shoeprints of Real-val, we evaluate the quality of predicted depth, thresholding which produces predicted prints. The evaluation essentially requires measuring the match between two binary maps. Therefore, we turn to

the *Intersection-over-Union* (IoU) as the metric. Note that a predicted depth map can generate various shoeprints depending on the threshold. We are motivated to develop a threshold-free metric based on IoU.

First, we get the (per-pixel) local average for predicted depth (d_{local}). This is essentially a highly blurred version of the predicted depth map (\hat{d}_R). Let us assume \hat{d}_R has lower values in the contact surface and higher values in the non-contact surface. Intuitively, regions where \hat{d}_R is lower than d_{local} touch the ground, and therefore leave a print. To get the shoeprint prediction closest to ground-truth, we sweep over a range of values of t and find the one for which IoU between $\hat{d}_R < td_{local}$ and ground-truth shoeprint is the highest. We set $shoeprint = \hat{d}_R < td_{local}$ for our chosen t .

This predicted print generally represents the ground-truth shoeprint well. However, it can cause issues for very large contact or non-contact surfaces. To understand this better, consider a shoe-sole with a large non-contact surface. The local average d_{local} in the middle of this non-contact surface may be quite high and thus even a large value for \hat{d}_R can be less than td_{local} indicating a contact surface. To solve this issue, we perform a sweep through values for t_{nc} and find the one for which IoU between $shoeprint \text{ AND } (\hat{d}_R < t_{nc})$ and ground-truth shoeprint is the highest and set $shoeprint = shoeprint \text{ AND } (\hat{d}_R < t_{nc})$. Similarly, this issue can also arise for large contact surfaces and we solve it by finding t_c for which IoU between $shoeprint \text{ OR } (\hat{d}_R < t_c)$ and ground-truth shoeprint is the highest and set $shoeprint = shoeprint \text{ OR } (\hat{d}_R < t_c)$. This is our final shoeprint prediction. Details on values for window-size to average over and thresholds are in the supplement.

4 Methodology

In this paper, we present a framework to predict depth from real images using unsupervised adversarial domain adaptation and intrinsic image decomposition. Given synthetic images (I_S) with corresponding synthetic albedo (a_S), depth (d_S), normal (n_S), and light (l_S) labels, and unlabeled real images (I_R), our goal is to correctly predict the depth (d_R) from real images. Figure 1 shows an overview of our network architecture. The main components of our network are a translator ($G_{S \rightarrow R}$) to stylize synthetic images as real images, a decomposer (f_R) to predict intrinsic decompositions, and a renderer (R) to reconstruct the real images from their decompositions.

Synthetic-only Training. First, we train a decomposer (f_S) only on synthetic data with paired ground-truth decompositions. Specifically, we use L1 loss over albedo, depth, and normal predictions and for the K -way classification of light, we use a cross entropy loss. Formally,

$$f_S(I_S) = \hat{a}_S, \hat{d}_S, \hat{n}_S, \hat{l}_S \quad (1)$$

$$\mathcal{L}_{sup}(f_S, I_S, a_S, d_S, n_S, l_S, \lambda_{int}) = \lambda_l \mathcal{L}_{CE}(\hat{l}_S, l_S) + \sum_{X \in \{a, d, n\}} \lambda_X \mathcal{L}_1(\hat{X}_S, X_S) \quad (2)$$

where \mathcal{L}_1 is the L1 loss, \mathcal{L}_{CE} is the K -way cross entropy loss and $\lambda_{int} = (\lambda_a, \lambda_d, \lambda_n, \lambda_l)$ are the weights for each intrinsic loss. Even though we aim to learn depth prediction, we use albedo, normal, and light as auxiliary data because such synthetic data is easy to obtain and we find that it helps our model learn better depth estimates presumably by detangling information in the input images into albedo, depth, normal, and light. Note that although we use a classification representation for light, our approach can easily be extended to other light representations such as an environment map, spherical gaussians, or spherical harmonics.

Domain Gaps. A model trained only on synthetic data is not expected to perform well when tested on real data. This can be attributed to the low-level and high-level domain gap between the two domains. The low-level domain gap comes from differences in appearance. The high-level domain gap can come from higher levels of detail and structural differences in the real domain. For example, our synthetic shoes mainly have two dominant depth layers (contact surfaces and non-contact surfaces) while real shoes tend to have a more uniform depth distribution and more precise detailing.

Image Translation. Previous work [26,70] handle low-level domain shift by translating images from the source domain to the target domain before feeding them to a network. We follow a similar approach and stylize our synthetic images as real images using a generative adversarial network. A generator $G_{S \rightarrow R}$ translates images from the synthetic domain to the real domain. The translated image is then fed into another generator $G_{R \rightarrow S}$ which translates it back to the synthetic domain. Discriminators D_R and D_S judge whether the image is from the real domain or the synthetic domain and helps the generators make better translations. A cycle loss between the original and reconstructed synthetic image ensures that structure and content are preserved during this stylizing process. This process is repeated in the other direction where real images are translated to the synthetic domain and then translated back again. These correspond to the loss functions

$$\mathcal{L}_{GAN}(G_{S \rightarrow R}, D_R, I_R, I_S) = \log D_R(I_R) + \log(1 - D_R(G_{S \rightarrow R}(I_S))) \quad (3)$$

$$\mathcal{L}_{tran} = \mathcal{L}_{GAN}(G_{S \rightarrow R}, D_R, I_R, I_S) + \mathcal{L}_{GAN}(G_{R \rightarrow S}, D_S, I_S, I_R) \quad (4)$$

$$\begin{aligned} \mathcal{L}_{cyc}(G_{S \rightarrow R}, G_{R \rightarrow S}, I_S, I_R) &= \mathcal{L}_1(G_{R \rightarrow S}(G_{S \rightarrow R}(I_S)) - I_S) \\ &\quad + \mathcal{L}_1(G_{S \rightarrow R}(G_{R \rightarrow S}(I_R)) - I_R) \end{aligned} \quad (5)$$

We feed the translated synthetic data to our pretrained decomposer and use synthetic labels to fine-tune f_R with $\mathcal{L}_{sup}(f_R, G_{S \rightarrow R}(I_S), a_S, d_S, n_S, l_S, \lambda_{int})$.

Image Reconstruction. In order to bridge the high-level domain gap between the synthetic and real data, we learn from unlabeled real data with a re-rendering loss. We use a differentiable, in-network renderer (R) for this purpose. The render takes intrinsic decompositions (albedo, depth, normal, and light) as input and outputs a predicted rendered image.

$$R(a_S, d_S, n_S, l_S) = \hat{I}_S \quad (6)$$

We first train R on synthetic data using $\mathcal{L}_1(R(a_S, d_S, n_S, l_S), I_S)$, and then



Fig. 4. Generating pseudo albedo maps from shoe-sole images. We show two pairs. We run mean-shift algorithm [18] on a shoe-sole image to group RGB pixels, resulting in the corresponding pseudo albedo map. We use the pseudo albedo maps as supervision signals to train the decomposer (cf. Figure 1).

finetune on translated synthetic data with $\mathcal{L}_1(R(a_S, d_S, n_S, l_S), G_{S \rightarrow R}(I_S))$. It thus learns to encode the physics behind image synthesis from intrinsic components. The trained renderer is frozen and used to reconstruct real images from their albedo, depth, normal, and light predictions ($\hat{a}_R, \hat{d}_R, \hat{n}_R, \hat{l}_R$) in our main pipeline. Thus, we learn from unlabeled real images using reconstruction loss

$$\mathcal{L}_{rec}(R, I_R, \hat{a}_R, \hat{d}_R, \hat{n}_R, \hat{l}_R) = \mathcal{L}_1(R(\hat{a}_R, \hat{d}_R, \hat{n}_R, \hat{l}_R), I_R) \quad (7)$$

The reason for freezing the renderer is to avoid drift; we want the *decomposer* to learn decompositions of real images that reconstruct the original image when passed through a renderer.

Pseudo Ground-truth Albedo. Shoe-soles, like many other man-made objects (such as cars, planes, etc) often have piece-wise constant albedos. We build on this idea and create pseudo ground-truth labels for our real data. Essentially, we group real image pixels using the non-parametric mean-shift clustering algorithm [18] to get our pseudo ground-truth albedo labels. Figure 4 shows example pseudo albedo on two real shoes. Note that this pseudo albedo is only an estimate and not the ground-truth. Therefore, it cannot be used in place of real image albedo prediction. This gives our real image albedo loss

$$\mathcal{L}_{alb}(\hat{a}_R, I_R) = \mathcal{L}_1(\hat{a}_R, pseudo_albedo(I_R)) \quad (8)$$

where *pseudo_albedo* groups pixels in I_R to predict the pseudo albedo labels.

Feature Alignment. Another method to perform low-level domain adaptation is feature alignment. A discriminator (D_{feat}) pushes the decomposer to generate similar features for the real and translated synthetic images. This encourages the decomposer outputs from real shoes to look similar to the outputs from synthetic shoes, which in turn produces better reconstructions when passed through the renderer. Feature alignment is learned using

$$\mathcal{L}_{feat}(f_R, D_{feat}, G_{S \rightarrow R}, I_S, I_R) = \mathcal{L}_{GAN}(f_R, D_{feat}, f_S(G_{S \rightarrow R}(I_S)), I_R) \quad (9)$$

Stage-wise Training. Although in practice all the losses can be minimized together, we choose to train in stages due to difficulties in training jointly (such as high memory usage, bad local minima, etc). We propose the following 4 stage training strategy. First, we train the decomposer (f_S) and renderer (R) only on synthetic data. Second, we train our image translation generators and corresponding discriminators ($G_{S \rightarrow R}$, $G_{R \rightarrow S}$, D_R , and D_S) using \mathcal{L}_{tran} and \mathcal{L}_{cyc} with weights λ_{tran} and λ_{cyc} respectively. Third, translated images from $G_{S \rightarrow R}$

are used to finetune R . Finally, with both R and $G_{S \rightarrow R}$ frozen, we finetune the decomposer f_R (initialized as f_S) using \mathcal{L}_{sup} , \mathcal{L}_{rec} , \mathcal{L}_{alb} and \mathcal{L}_{feat} with weights λ_{sup} , λ_{rec} , λ_{alb} and λ_{feat} respectively on translated synthetic images and real images.

5 Experiments

We carry out extensive experiments on our benchmark, comparing various methods of domain adaptation and intrinsic decomposition tailored to shoeprint prediction. We start with the implementation details, followed by visual comparison and quantitative comparison. We also include an ablation study to analyze why our *ShoeRinsics* outperforms other approaches.

5.1 Implementation

We choose an image resolution of 405x765. Since this is quite high, we train on patches of size 128x128 instead of the whole image. The patch positions are random and determined on the fly during training. This allows us to fit more diverse image samples per optimizer step.

Our decomposer (f_S) and renderer (R) have a classic encoder-decoder structure as used in [29]. We modify the light prediction decoder to output a 17-way classification to reflect our training dataset and add residual connections between layers. Our generators and discriminators ($G_{S \rightarrow R}$, $G_{R \rightarrow S}$, D_R , D_S and D_{feat}) have the same structure as used in [26]. We modify D_{feat} to add a similar additional branch with input dimension 17 to process light features. D_{feat} takes in the concatenation of the albedo, depth, and normal features as one input and the light features as the second input, and outputs the concatenated results from all intrinsic components. We also modify D_{feat} to use a kernel size of 3 to process the albedo, depth, and normal features since the added context helps it discriminate between synthetic and real features more easily. We use Adam optimizer to train all models and set the learning rate as 1e-3 and 1e-4 for training models from scratch and finetuning respectively.

We train our model in stages as proposed in Section 4. The decomposer (f_S) is trained in the first stage using $\lambda_{int} = (1, 1, 1, 0.1)$. We train our image translation generator and discriminators as done in [26] using $\lambda_{tran} = \lambda_{cyc} = 1$. In the final stage, we set $\lambda_{sup} = 1$, $\lambda_{rec} = 3$, $\lambda_{alb} = 2$, $\lambda_{feat} = 1$ and $\lambda_{int} = (1, 2, 1, 0.1)$. We additionally use a weight decay factor of 0.9 every 1000 optimizer steps on synthetic albedo, normal, and light supervision weights (λ_a , λ_n , λ_l) to focus more on depth predictions. Training is run for 20M optimizer steps in the first 2 stages and for 100K optimizer steps in the last 2 stages using a batch size of 8.

For a fair comparison between models, we ensure that all models follow patch-based training on the same image resolution and train for the same number of optimizer steps.

During testing, we compare test-time augmentation following [15, 25]. For each image, we produce 23 variants: 3 flips (horizontal, vertical, and vertical+horizontal), 4 rotations (angles $+5^\circ$, $+10^\circ$, -5° , and -10°), 4 scalings (scale

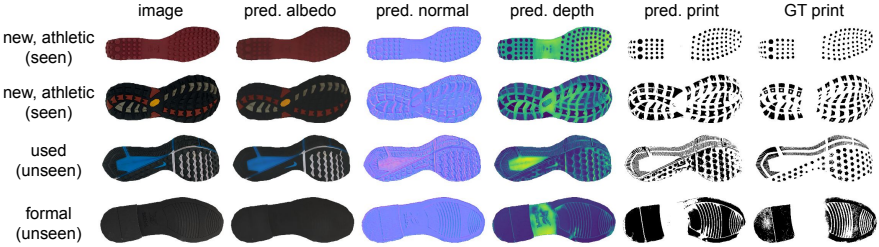


Fig. 5. Visualization of predicted shoeprints, as well as intrinsics, by our *ShoeRinsics* on Real-val. *ShoeRinsics* produces visually appealing intrinsic decompositions (depth, albedo, and normal), and shoeprints on both seen and unseen shoe categories. Shoeprint predictions are obtained by thresholding depth predictions as described in Section 3.5.

factor 0.5, 0.8, 1.5, and 1.8), and 12 flip+rotation versions (three flips times four rotations). For each variant, we predict the depth and transform it according to the original testing image. We average 24 depth maps as the final prediction.

5.2 Qualitative Results of *ShoeRinsics*

We visualize our model predictions on Real-val with ground-truth print in Figure 6. Our model predicts good depth maps which translate to shoeprints that are very close to the ground-truth in the absence of any ground-truth on real images. As a bonus, we are also able to make visually appealing predictions on other intrinsic components. We provide more qualitative results in the supplement for the Real-test dataset without ground-truth.

5.3 State-of-the-art Comparison

We compare with [29] which performs classic intrinsic image decomposition on objects. The main difference between our work and this line of work is that we do explicit domain adaptation on the image and feature space in addition to intrinsic image decomposition. This helps us bridge the low-level domain gap between synthetic and real images. We see from our experimental results in Table 2 that by including these extra modules *ShoeRinsics* increases IoU on the known category (new athletic shoes) by 68.3% and new unseen categories by 20.4% on formal shoes and 46.7% on used shoes. Note that [29] predicts normals only as shape. We use the standard Frankot Chellappa algorithm [16] to integrate the normals and obtain depth maps.

Our model outperforms work on domain adaptation [55,20,26] since we learn image decomposition into all the intrinsic components (albedo, depth, normal, and light) in addition to domain adaptation. This helps us distinguish depth features from non-depth features. More importantly, the intrinsic components are put together through a rendering module which helps our model reason about the high-level structure in real images. Qualitative comparison in Figure 6 show that the most pronounced effect of our rendering module is overall consistency and more attention to structural detail. It makes sense that an irregular depth

Table 2. Benchmarking on Real-val. We use IoU as the metric, break down the analysis for different shoe categories (new athletic shoes which are seen during training, and formal and used shoes unseen in training). We compute mean IoU over all validation examples. Our *ShoeRinsics* performs the best on both seen and unseen categories, clearly demonstrating the benefit of combining synthetic-to-real domain adaptation with intrinsic decomposition. The bottom panel shows that our *ShoeRinsics*, which incorporates discriminator, translator and renderer, significantly boosts performance from 38.4% (syn-only, depth only) to 46.8% meanIoU, outperforming the state-of-the-art methods shown in the upper panel. Furthermore, exploiting test-time augmentation brings another boost to 49.0% meanIoU.

<i>Method</i>	<i>New, Athletic</i>	<i>Formal</i>	<i>Used</i>	<i>meanIoU</i>
RIN [29]	30.0	39.7	24.4	30.4
ADDA [55]	46.5	41.4	27.2	41.4
UDAB [20]	46.0	40.4	29.6	41.4
CyCADA [26]	48.8	43.9	34.5	44.8
syn-only, depth only	41.3	41.2	28.4	38.4
syn-only, all intrinsics	41.8	41.5	27.1	38.5
ShoeRinsics	50.5	47.8	35.8	46.8
w/o discriminator	48.2	39.9	33.6	43.6
w/o translator	49.0	42.8	31.4	44.0
w/o renderer	49.0	46.4	34.7	45.4
ShoeRinsics w/ test-time aug	52.4	52.9	36.9	49.0

prediction would not pass through the rendering module to reconstruct the input image well. Structural details are picked up for a similar reason. When tested on IoU, *ShoeRinsics* outperform the best work on domain adaptation on both seen and unseen categories as shown in Table 2. We note that the higher performance gap occurs in the unseen category which indicates that *ShoeRinsics* is better at reasoning about new shoe structures. When exploiting test-time augmentation (cf. *ShoeRinsics* w/ test-time aug), we boost the performance from meanIoU=46.8 to 49.0.

5.4 Ablation Study

We perform extensive experiments to show the effects of each module. We see in Table 2 that each of the modules play a role in improving performance.

Ablation *syn-only, depth only* and *syn-only, all intrinsics* are decomposers trained purely on synthetic data. The former only predicts the depth while the latter predicts albedo, normal, and light as well. *Syn-only, all intrinsics* achieves better performance than *syn-only, depth only* due to the additional supervision on the other intrinsics. Results on these models serve as a baseline to compare improvement made by our efforts to learn from real data.

ShoeRinsics w/o discriminator has all the components of our final model except for the feature discriminator D_{feat} . The drop in IoU from our final model suggests that D_{feat} helps the decomposer f_R predict more likely depth maps by forcing it to output similar predictions for the synthetic and the real domain.

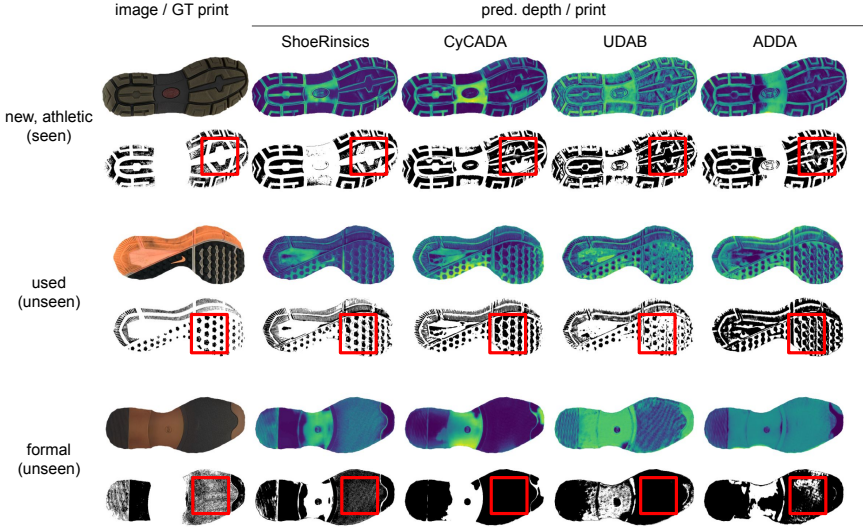


Fig. 6. Comparison with the state-of-the-art methods of domain adaptation tailored to depth prediction on our Real-val benchmark. Our ShoeRinsics performs better than others for both seen and unseen shoe categories as shown by the red boxes.

ShoeRinsics w/o translator runs on our full setup but skips translating synthetic images as real images. We see an improvement in IoU in our final model by adding the translation module. Also, comparing this to *syn-only, all intrinsics* which learns all intrinsic components only from synthetic data, we see the expected boost in performance when learning with intrinsic image decomposition and feature alignment from real data.

ShoeRinsics w/o renderer is comparable to CyCADA [26] except that it performs image decomposition into all the intrinsic components instead of just depth. We see that with this extra information the model already gets a small boost in performance as it is more aware of the image features that contribute to depth and the ones that do not. A more pronounced improvement is seen in our final model which suggests the necessity of the renderer.

To validate our design choice of training in patches, we train our decomposer on full-sized synthetic images only and compare to *syn-only, all intrinsics* which is a similar setup trained using patches. We find that the full-sized approach yields a mean IoU of 36.5% while the patch-based method yields a mean IoU of 38.5% as shown in Table 2, showing the superiority of patch-based training in this setup.

5.5 Failure Cases

We note that our model performs most poorly on shoes with complex materials as depicted in Figure 7. This is because Syn-train does not contain any complex materials and we use a piece-wise constant pseudo albedo supervision on Real-train. Future work may explore richer synthetic datasets and other ways to guide albedo predictions on real data to mitigate this issue.



Fig. 7. Failure cases on Real-test. *ShoeRinsics* performs poorly in the presence of complex materials. This shows a venue to improve in future work.

6 Conclusion

We have formulated an approach for training a model which predicts shoe tread intrinsics from readily available commercial photographs. This leverages a combination of synthetic training data, domain adaptation, and self-supervised re-rendering criteria. This yields shoe print predictions which we have validated using a held-out collection of tread photos and ground-truth impressions. These results offer a promising approach to automatically constructing a comprehensive database of shoe pseudo-impressions which can serve the needs of footwear examiners and researchers.

Acknowledgements. This work was funded by the Center for Statistics and Applications in Forensic Evidence (CSAFE) through Cooperative Agreements, 70NANB15H176 and 70NANB20H019.

References

1. 6pm, <http://www.6pm.com/> 7
2. Footwear reference database for identifying scene of crime shoeprints. <http://www.fosterfreeman.com/trace-evidence/357-sicar-6-solemate-2.html>, accessed: 2022-03-01 2
3. Zappos, <http://www.zappos.com/> 7
4. Ahmadyan, A., Zhang, L., Ablavatski, A., Wei, J., Grundmann, M.: Objectron: A large scale dataset of object-centric videos in the wild with pose annotations. In: Proceedings of the IEEE/CVF Conference on Computer Vision and Pattern Recognition. pp. 7822–7831 (2021) 5
5. AlGarni, G., Hamiane, M.: A novel technique for automatic shoeprint image retrieval. *Forensic science international* **181**(1-3), 10–14 (2008) 2
6. Alhaija, H.A., Mustikovela, S.K., Thies, J., Jampani, V., Nießner, M., Geiger, A., Rother, C.: Intrinsic autoencoders for joint neural rendering and intrinsic image decomposition (2021) 4
7. Alizadeh, S., Kose, C.: Automatic retrieval of shoeprint images using blocked sparse representation. *Forensic science international* **277**, 103–114 (2017) 3
8. Almaadeed, S., Bouridane, A., Crookes, D., Nibouche, O.: Partial shoeprint retrieval using multiple point-of-interest detectors and sift descriptors. *Integrated Computer-Aided Engineering* **22**(1), 41–58 (2015) 3
9. Alp Guler, R., Trigeorgis, G., Antonakos, E., Snape, P., Zafeiriou, S., Kokkinos, I.: Densereg: Fully convolutional dense shape regression in-the-wild. In: Proceedings of the IEEE Conference on Computer Vision and Pattern Recognition. pp. 6799–6808 (2017) 4

10. Baig, M.H., Torresani, L.: Coupled depth learning. In: 2016 IEEE Winter Conference on Applications of Computer Vision (WACV). pp. 1–10. IEEE (2016) 4
11. Bodziak, W.J.: Footwear impression evidence: detection, recovery, and examination. CRC Press (2017) 1, 21
12. Bouridane, A., Alexander, A., Nibouche, M., Crookes, D.: Application of fractals to the detection and classification of shoeprints. In: Proceedings 2000 International Conference on Image Processing (Cat. No. 00CH37101). vol. 1, pp. 474–477. IEEE (2000) 2
13. De Chazal, P., Flynn, J., Reilly, R.B.: Automated processing of shoeprint images based on the fourier transform for use in forensic science. IEEE transactions on pattern analysis and machine intelligence 27(3), 341–350 (2005) 2
14. Duchon, J.: Splines minimizing rotation-invariant semi-norms in sobolev spaces. In: Constructive theory of functions of several variables, pp. 85–100. Springer (1977) 7
15. Forsyth, D.A., Rock, J.J.: Intrinsic image decomposition using paradigms. CoRR abs/2011.10512 (2020), <https://arxiv.org/abs/2011.10512> 11
16. Frankot, R.T., Chellappa, R.: A method for enforcing integrability in shape from shading algorithms. IEEE Transactions on pattern analysis and machine intelligence 10(4), 439–451 (1988) 12, 24, 25
17. Fu, H., Gong, M., Wang, C., Batmanghelich, K., Tao, D.: Deep ordinal regression network for monocular depth estimation. In: Proceedings of the IEEE conference on computer vision and pattern recognition. pp. 2002–2011 (2018) 4
18. Fukunaga, K., Hostetler, L.: The estimation of the gradient of a density function, with applications in pattern recognition. IEEE Transactions on information theory 21(1), 32–40 (1975) 6, 10, 26
19. Furukawa, R., Sagawa, R., Kawasaki, H.: Depth estimation using structured light flow—analysis of projected pattern flow on an object’s surface. In: Proceedings of the IEEE International Conference on Computer Vision. pp. 4640–4648 (2017) 4
20. Ganin, Y., Lempitsky, V.: Unsupervised domain adaptation by backpropagation. In: Bach, F., Blei, D. (eds.) Proceedings of the 32nd International Conference on Machine Learning. Proceedings of Machine Learning Research, vol. 37, pp. 1180–1189. PMLR, Lille, France (07–09 Jul 2015), <https://proceedings.mlr.press/v37/ganin15.html> 4, 12, 13, 23, 24
21. Garg, R., Bg, V.K., Carneiro, G., Reid, I.: Unsupervised cnn for single view depth estimation: Geometry to the rescue. In: European conference on computer vision. pp. 740–756. Springer (2016) 4
22. Gueham, M., Bouridane, A., Crookes, D.: Automatic recognition of partial shoeprints based on phase-only correlation. In: 2007 IEEE International Conference on Image Processing. vol. 4, pp. IV–441. IEEE (2007) 2
23. Gueham, M., Bouridane, A., Crookes, D.: Automatic classification of partial shoeprints using advanced correlation filters for use in forensic science. In: 2008 19th International Conference on Pattern Recognition. pp. 1–4. IEEE (2008) 2
24. Gueham, M., Bouridane, A., Crookes, D., Nibouche, O.: Automatic recognition of shoeprints using fourier-mellin transform. In: 2008 NASA/ESA Conference on Adaptive Hardware and Systems. pp. 487–491. IEEE (2008) 2
25. He, K., Zhang, X., Ren, S., Sun, J.: Deep residual learning for image recognition. In: Proceedings of the IEEE conference on computer vision and pattern recognition. pp. 770–778 (2016) 11
26. Hoffman, J., Tzeng, E., Park, T., Zhu, J.Y., Isola, P., Saenko, K., Efros, A., Darrell, T.: CyCADA: Cycle-consistent adversarial domain adaptation. In: Dy, J., Krause,

- A. (eds.) Proceedings of the 35th International Conference on Machine Learning. Proceedings of Machine Learning Research, vol. 80, pp. 1989–1998. PMLR (10–15 Jul 2018), <https://proceedings.mlr.press/v80/hoffman18a.html> 4, 9, 11, 12, 13, 14, 23, 24
27. Hoiem, D., Efros, A.A., Hebert, M.: Automatic photo pop-up. In: ACM SIGGRAPH 2005 Papers, pp. 577–584 (2005) 4
 28. Jakob, W.: Mitsuba renderer (2010), <http://www.mitsuba-renderer.org> 6
 29. Janner, M., Wu, J., Kulkarni, T.D., Yildirim, I., Tenenbaum, J.B.: Self-supervised intrinsic image decomposition. In: Proceedings of the 31st International Conference on Neural Information Processing Systems. p. 5938–5948. NIPS’17, Curran Associates Inc., Red Hook, NY, USA (2017) 4, 11, 12, 13, 24, 25
 30. Jing, M.Q., Ho, W.J., Chen, L.H.: A novel method for shoeprints recognition and classification. In: 2009 International conference on machine learning and cybernetics. vol. 5, pp. 2846–2851. IEEE (2009) 2
 31. Kendall, A., Gal, Y.: What uncertainties do we need in bayesian deep learning for computer vision? Advances in neural information processing systems 30 (2017) 4
 32. Kong, B., Supancic, J., Ramanan, D., Fowlkes, C.C.: Cross-domain image matching with deep feature maps. International Journal of Computer Vision 127(11), 1738–1750 (2019) 2, 3
 33. Kortylewski, A., Vetter, T.: Probabilistic compositional active basis models for robust pattern recognition. In: BMVC (2016) 2, 3
 34. Krig, S.: Interest point detector and feature descriptor survey. In: Computer vision metrics, pp. 187–246. Springer (2016) 3
 35. Kuznetsov, Y., Stuckler, J., Leibe, B.: Semi-supervised deep learning for monocular depth map prediction. In: Proceedings of the IEEE conference on computer vision and pattern recognition. pp. 6647–6655 (2017) 4
 36. Laina, I., Rupprecht, C., Belagiannis, V., Tombari, F., Navab, N.: Deeper depth prediction with fully convolutional residual networks. In: 2016 Fourth international conference on 3D vision (3DV). pp. 239–248. IEEE (2016) 4
 37. Li, J., Klein, R., Yao, A.: A two-streamed network for estimating fine-scaled depth maps from single rgb images. In: Proceedings of the IEEE International Conference on Computer Vision. pp. 3372–3380 (2017) 4
 38. Li, Z., Snavely, N.: Megadepth: Learning single-view depth prediction from internet photos. In: Proceedings of the IEEE Conference on Computer Vision and Pattern Recognition. pp. 2041–2050 (2018) 4
 39. Li, Z., Shafiei, M., Ramamoorthi, R., Sunkavalli, K., Chandraker, M.: Inverse rendering for complex indoor scenes: Shape, spatially-varying lighting and svbrdf from a single image. In: Proceedings of the IEEE/CVF Conference on Computer Vision and Pattern Recognition. pp. 2475–2484 (2020) 4
 40. Long, M., Ding, G., Wang, J., Sun, J., Guo, Y., Yu, P.S.: Transfer sparse coding for robust image representation. In: Proceedings of the IEEE conference on computer vision and pattern recognition. pp. 407–414 (2013) 4
 41. Ma, Z., Ding, Y., Wen, S., Xie, J., Jin, Y., Si, Z., Wang, H.: Shoe-print image retrieval with multi-part weighted cnn. IEEE Access 7, 59728–59736 (2019) 3
 42. Nestmeyer, T., Lalonde, J.F., Matthews, I., Lehrmann, A.: Learning physics-guided face relighting under directional light. In: Proceedings of the IEEE/CVF Conference on Computer Vision and Pattern Recognition. pp. 5124–5133 (2020) 4
 43. Ranftl, R., Lasinger, K., Hafner, D., Schindler, K., Koltun, V.: Towards robust monocular depth estimation: Mixing datasets for zero-shot cross-dataset transfer. IEEE transactions on pattern analysis and machine intelligence (2020) 4

44. Ranftl, R., Vineet, V., Chen, Q., Koltun, V.: Dense monocular depth estimation in complex dynamic scenes. In: Proceedings of the IEEE conference on computer vision and pattern recognition. pp. 4058–4066 (2016) 4
45. Rida, I., Fei, L., Proença, H., Nait-Ali, A., Hadid, A.: Forensic shoe-print identification: a brief survey. arXiv preprint arXiv:1901.01431 (2019) 3
46. Roy, A., Todorovic, S.: Monocular depth estimation using neural regression forest. In: Proceedings of the IEEE conference on computer vision and pattern recognition. pp. 5506–5514 (2016) 4
47. Saxena, A., Chung, S., Ng, A.: Learning depth from single monocular images. Advances in neural information processing systems **18** (2005) 4
48. Saxena, A., Chung, S.H., Ng, A.Y.: 3-d depth reconstruction from a single still image. International journal of computer vision **76**(1), 53–69 (2008) 4
49. Sengupta, S., Gu, J., Kim, K., Liu, G., Jacobs, D.W., Kautz, J.: Neural inverse rendering of an indoor scene from a single image. In: International Conference on Computer Vision (ICCV) (2019) 4
50. Sengupta, S., Kanazawa, A., Castillo, C.D., Jacobs, D.W.: Sfsnet: Learning shape, reflectance and illuminance of faces in the wild. In: Computer Vision and Pattern Recognition (CVPR) (2018) 4
51. Shin, D., Ren, Z., Sudderth, E.B., Fowlkes, C.C.: 3d scene reconstruction with multi-layer depth and epipolar transformers. In: Proceedings of the IEEE/CVF International Conference on Computer Vision. pp. 2172–2182 (2019) 4
52. Srinivasan, P.P., Deng, B., Zhang, X., Tancik, M., Mildenhall, B., Barron, J.T.: Nerv: Neural reflectance and visibility fields for relighting and view synthesis. In: CVPR (2021) 4
53. Sun, B., Saenko, K.: Deep coral: Correlation alignment for deep domain adaptation. In: European conference on computer vision. pp. 443–450. Springer (2016) 4
54. Tsai, Y.H., Hung, W.C., Schuler, S., Sohn, K., Yang, M.H., Chandraker, M.: Learning to adapt structured output space for semantic segmentation. In: Proceedings of the IEEE conference on computer vision and pattern recognition. pp. 7472–7481 (2018) 4
55. Tzeng, E., Hoffman, J., Saenko, K., Darrell, T.: Adversarial discriminative domain adaptation. In: 2017 IEEE Conference on Computer Vision and Pattern Recognition (CVPR). pp. 2962–2971 (2017). <https://doi.org/10.1109/CVPR.2017.316> 4, 12, 13, 23, 24
56. Tzeng, E., Hoffman, J., Zhang, N., Saenko, K., Darrell, T.: Deep domain confusion: Maximizing for domain invariance. arXiv preprint arXiv:1412.3474 (2014) 4
57. Wang, X., Zhang, C., Wu, Y., Shu, Y.: A manifold ranking based method using hybrid features for crime scene shoeprint retrieval. Multimedia Tools and Applications **76**(20), 21629–21649 (2017) 2, 3
58. Wang, Z., Yu, X., Lu, M., Wang, Q., Qian, C., Xu, F.: Single image portrait relighting via explicit multiple reflectance channel modeling. ACM Trans. Graph. **39**(6) (Nov 2020). <https://doi.org/10.1145/3414685.3417824> 4
59. Wu, S., Makadia, A., Wu, J., Snively, N., Tucker, R., Kanazawa, A.: De-rendering the world’s revolutionary artefacts. In: CVPR (2021) 4
60. Xie, J., Girshick, R., Farhadi, A.: Deep3d: Fully automatic 2d-to-3d video conversion with deep convolutional neural networks. In: European conference on computer vision. pp. 842–857. Springer (2016) 4
61. Yin, W., Liu, Y., Shen, C., Yan, Y.: Enforcing geometric constraints of virtual normal for depth prediction. In: Proceedings of the IEEE/CVF International Conference on Computer Vision. pp. 5684–5693 (2019) 4

62. Yongjie Zhu, Yinda Zhang, S.L., Shi, B.: Spatially-varying outdoor lighting estimation from intrinsics. In: CVPR (2021) 4
63. Yu, Y., Meka, A., Elgharib, M., Seidel, H.P., Theobalt, C., Smith, W.: Self-supervised outdoor scene relighting. In: European Conference on Computer Vision (ECCV) (2020) 4
64. Zhang, K., Luan, F., Wang, Q., Bala, K., Snavely, N.: Physg: Inverse rendering with spherical gaussians for physics-based material editing and relighting. In: The IEEE/CVF Conference on Computer Vision and Pattern Recognition (CVPR) (2021) 4
65. Zhang, Y., Fu, H., Dellandréa, E., Chen, L.: Adapting convolutional neural networks on the shoeprint retrieval for forensic use. In: Chinese Conference on Biometric Recognition. pp. 520–527. Springer (2017) 2, 3
66. Zhao, Y., Kong, S., Fowlkes, C.: Camera pose matters: Improving depth prediction by mitigating pose distribution bias. In: Proceedings of the IEEE/CVF Conference on Computer Vision and Pattern Recognition. pp. 15759–15768 (2021) 4
67. Zhao, Y., Kong, S., Shin, D., Fowlkes, C.: Domain decluttering: Simplifying images to mitigate synthetic-real domain shift and improve depth estimation. In: Proceedings of the IEEE/CVF Conference on Computer Vision and Pattern Recognition. pp. 3330–3340 (2020) 4
68. Zheng, C., Cham, T.J., Cai, J.: T2net: Synthetic-to-realistic translation for solving single-image depth estimation tasks. In: Proceedings of the European Conference on Computer Vision (ECCV). pp. 767–783 (2018) 4
69. Zhou, H., Yu, X., Jacobs, D.: Glosh: Global-local spherical harmonics for intrinsic image decomposition. In: 2019 IEEE/CVF International Conference on Computer Vision (ICCV). pp. 7819–7828 (2019). <https://doi.org/10.1109/ICCV.2019.00791> 4
70. Zhu, J.Y., Park, T., Isola, P., Efros, A.A.: Unpaired image-to-image translation using cycle-consistent adversarial networks. In: Proceedings of the IEEE international conference on computer vision. pp. 2223–2232 (2017) 4, 9

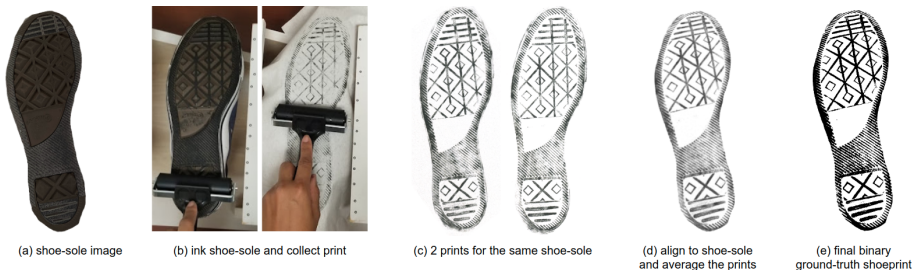


Fig. 8. Flowchart for collecting ground-truth shoeprints from shoes in Real-val. (a) shows an example shoe. The shoe is painted with a thin layer of relief ink and a paper is pressed evenly onto the shoe-sole using a roller in (b). This method is repeated to get 2-3 different prints for the same shoe as shown in (c). These prints are aligned to the shoe-sole using thin plate spline and averaged to get a print with more even coverage. The final binary ground-truth shoeprint shown in (e) is obtained by thresholding (d).

Appendices

We propose a novel method (*ShoeRinsics*) which incorporates synthetic-to-real domain adaptation and intrinsic image decomposition to learn depth estimation from labeled synthetic data and unlabeled real data. We apply our method to estimate depth on real shoe-sole images and threshold the depth predictions to get shoeprint predictions. We test our method by setting up an evaluation protocol and comparing our shoeprint predictions to ground-truth shoeprints we collected from a set of real shoes. *ShoeRinsics* remarkably outperforms state-of-the-art methods on domain adaptation and intrinsic image decomposition. In this supplementary material, we discuss the following topics

- Section 7 demonstrates how we collect ground-truth shoeprints from a collection of shoes.
- Section 8 discusses details on the process of thresholding depth predictions to obtain shoeprint prediction.
- Section 9 shows visualization of our predictions on Real-test images downloaded from the internet.
- Section 10 compares our predictions to those of RIN.
- Section 11 details our network architecture.
- Section 12 discusses how we obtain pseudo albedo labels on real images.
- Section 13 visualizes the different lighting configurations in our synthetic dataset.

7 Collecting Ground-truth Shoeprints

We summarize the process of collecting ground-truth shoeprint for shoes in Real-val in Figure 8. Real-val consist of both used and new shoes. The new shoes are collected from thrift stores which often sell new or very lightly used shoes. We

first clean all the shoe-soles with soap and water and let them dry. Next, we photograph the shoe-soles in a brightly lit environment. We put together 5 square light panels to create a light box and place the shoe on a holder inside the light box. We also illuminate the shoes using a ring light on top. After photographing the shoes we proceed to collecting prints from the shoe. We use a process called *block printing technique* which is widely used in forensics to collect lab shoeprint impressions [11]. With the shoe resting on the holder, we paint the shoe-sole with a thin layer of relief ink using a roller. Forgoing the roller and simply using a paint brush would cause ink blobs to get stuck in the nooks and crannies of the shoe-tread leading to blotchy prints. While the ink is still wet, we quickly press a slightly absorbent white paper onto the shoe-sole using a roller. The use of the roller distributes pressure throughout the paper and thus produces more uniform prints. We collect 2-3 sets of prints for each shoe, each time painting the shoe with a new layer of ink. Notice how these individual prints are not identical and contain areas of uneven coverage. To get a smoother result, we align all the prints to the shoe-sole image (using thin plate spline and point correspondences on the shoe-sole image and the collected prints) and average them. This average is a more complete and even. Finally, this average print is thresholded to get our binary ground-truth shoeprint.

8 From Depth Prediction to Shoeprint Prediction

We get the shoeprint prediction by thresholding the predicted depth (\hat{d}_R) of a shoe-sole image. However, different thresholds can produce different predicted shoeprints. So, we develop a threshold-free metric. Ideally, we want to threshold the depth prediction in a way that produces a shoeprint prediction that most closely matches the ground-truth shoeprint (S^*). We summarize our algorithm in Algorithm 1.

First, we determine a per-pixel local average (d_{local}) for the predicted depth. To obtain d_{local} we convolve \hat{d}_R with a square kernel of equal values such that the kernel sums to 1. We choose a relatively large kernel size of 45×45 to average over large areas. Thus, our kernel consists of constant values of $\frac{1}{45 \times 45}$. For comparison, our shoe-sole image and predicted depth map resolution is 405×765 . Additionally, we use a padding of 22 for convolution so that d_{local} has dimension equal to \hat{d}_R . We note that boundaries and invalid depth values outside the mask may cause artifacts in d_{local} . To negate this effect, we offset \hat{d}_R with $\min(\hat{d}_R)$ so that the new minimum value of \hat{d}_R is 0. We then set \hat{d}_R outside the mask equal to 0. d_{local} is determined after this initial fix on \hat{d}_R . Next, we get m_{local} by convolving the mask with the same kernel used for d_{local} and finally set $d_{local} = \frac{d_{local}}{m_{local}}$.

The depth maps have lower values in contact surfaces and higher values in non-contact surfaces. Our initial guess of the shoeprint is $\hat{d}_R < td_{local}$ for some threshold t . Theoretically, we want to sweep over all possible values of t and find the one which gives the highest IoU between $\hat{d}_R < td_{local}$ and the ground-truth

Algorithm 1 Shoeprint Matching from Depth

```

1: Input: predicted depth map  $\hat{d}_R$ , ground-truth shoeprint  $S^*$ , and mask  $m$ 
2: Initialize best-matching IoU  $v_{max} = 0$  and the derived shoeprint  $S_{optimal} = 0$ 
3:  $\hat{d}_R = \hat{d}_R - \min(\hat{d}_R)$ 
4: set  $\hat{d}_R[\text{NOT } m] = 0$ 
5: Initialize square kernel for convolution,  $kernel = \frac{\text{ones}(\text{shape}=(45,45))}{45 \times 45}$ 
6: determine local per-pixel depth  $d_{local} = \text{conv}(\hat{d}_R, kernel, pad = 22)$ 
7: determine  $m_{local} = \text{conv}(m, kernel, pad = 22)$ 
8:  $d_{local} = \frac{d_{local}}{m_{local}}$ 
9:
10: for  $t \in [0.1, 0.11, 0.12, \dots, 2)$  do
11:   determine shoeprint  $S_t = \hat{d}_R < td_{local}$ 
12:   calculate the IoU between  $S_t$  and  $S^*$ ,  $v_t = \text{IoU}(S_t, S^*)$ .
13:   if  $v_t > v_{max}$  then
14:      $v_{max} = v_t$ ,  $S_{optimal} = S_t$ 
15:   end if
16: end for
17:
18: sort  $\hat{d}_R$  and determine depth value at the 95th percentile  $d_{95}$ 
19: for  $t_{nc} \in [0.1d_{95}, 0.1d_{95} + 0.01, 0.1d_{95} + 0.02, \dots, d_{95})$  do
20:   determine shoeprint  $S_{t_{nc}} = S_{optimal}$  AND  $(\hat{d}_R < t_{nc})$ 
21:   calculate the IoU between  $S_{t_{nc}}$  and  $S^*$ ,  $v_{t_{nc}} = \text{IoU}(S_{t_{nc}}, S^*)$ .
22:   if  $v_{t_{nc}} > v_{max}$  then
23:      $v_{max} = v_{t_{nc}}$ ,  $S_{optimal} = S_{t_{nc}}$ 
24:   end if
25: end for
26:
27: sort  $\hat{d}_R$  and determine depth value at the 5th percentile  $d_{05}$ 
28: for  $t_c \in [d_{05}, d_{05} + 0.1, d_{05} + 0.2, \dots, 30d_{05})$  do
29:   determine shoeprint  $S_{t_c} = S_{optimal}$  OR  $(\hat{d}_R < t_c)$ 
30:   calculate the IoU between  $S_{t_c}$  and  $S^*$ ,  $v_{t_c} = \text{IoU}(S_{t_c}, S^*)$ .
31:   if  $v_{t_c} > v_{max}$  then
32:      $v_{max} = v_{t_c}$ ,  $S_{optimal} = S_{t_c}$ 
33:   end if
34: end for
35: return the derived shoeprint  $S_{optimal}$  and the IoU metric  $v_{max}$ 

```

print. Practically, we sample values from range $[0.1, 2)$ at intervals of 0.01. We set our predicted shoeprint $S_{optimal} = \hat{d}_R < td_{local}$

Although this shoeprint estimation is good enough for most cases, it will cause problems in very large non-contact surfaces. d_{local} will be very high in the middle of such regions. So, even a large depth value can be interpreted as a contact surface if it is lower than td_{local} . We fix this by identifying the threshold t_{nc} which gives the highest IoU between S^* and $S_{optimal}$ AND $(\hat{d}_R < t_{nc})$. We update our shoeprint prediction $S_{optimal}$ to be $S_{optimal}$ AND $(\hat{d}_R < t_{nc})$. A similar problem and solution applies for large contact surfaces. We find threshold

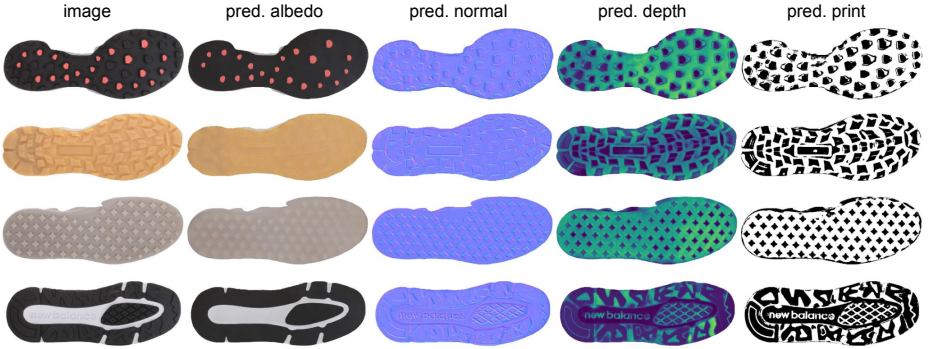


Fig. 9. Visualization of predicted shoeprints, as well as intrinsics, by our *ShoeRinsics* on Real-test. Real-test consists of images of real shoe-soles downloaded from online retailers. Visually, we can see our method works quite well w.r.t intrinsic decomposition (albedo, normal, and depth). Thresholding depth leads to predicted shoeprints, which visually look good.

t_c for which the IoU between S^* and $S_{optimal}$ OR ($\hat{d}_R < t_c$) is highest. Finally, we set $S_{optimal} = S_{optimal}$ OR ($\hat{d}_R < t_c$).

To find t_{nc} and t_c , we sort \hat{d}_R values on the shoe-sole and get the depth values at the 95th percentile (d_{95}) and the 5th percentile (d_{05}). After experimentation, we find that sampling t_{nc} from range $[0.1d^{95}, d^{95})$ at intervals of 0.01 and sampling t_c from range $[d^{05}, 30d^{05})$ at intervals of 0.1 is sufficient.

To visualize shoeprint predictions from real images without ground-truth shoeprint, we set $t = 1$, $t_c = \min(\hat{d}_R)$, and $t_{nc} = \max(\hat{d}_R)$.

9 Qualitative Results on Real-test

One of the datasets we collected, Real-test, consists of images of real shoe-soles downloaded from online retailers. These images do not come with any ground-truth labels. We show visualizations of albedo, normal, depth and print predictions from *ShoeRinsics* on the Real-test dataset in Figure 9. We see that the predictions are pleasing visually and the predicted print closely represents likely shoeprints from the respective shoe-sole images.

Additionally, we also compare our depth and print predictions on the Real-test dataset with that of state-of-the-art related work on domain adaptation [20,26,55] in Figure 10, clearly showing how our work improves on existing work. Notably, *ShoeRinsics* is able to predict more uniform structure and picks up more details than the related work.

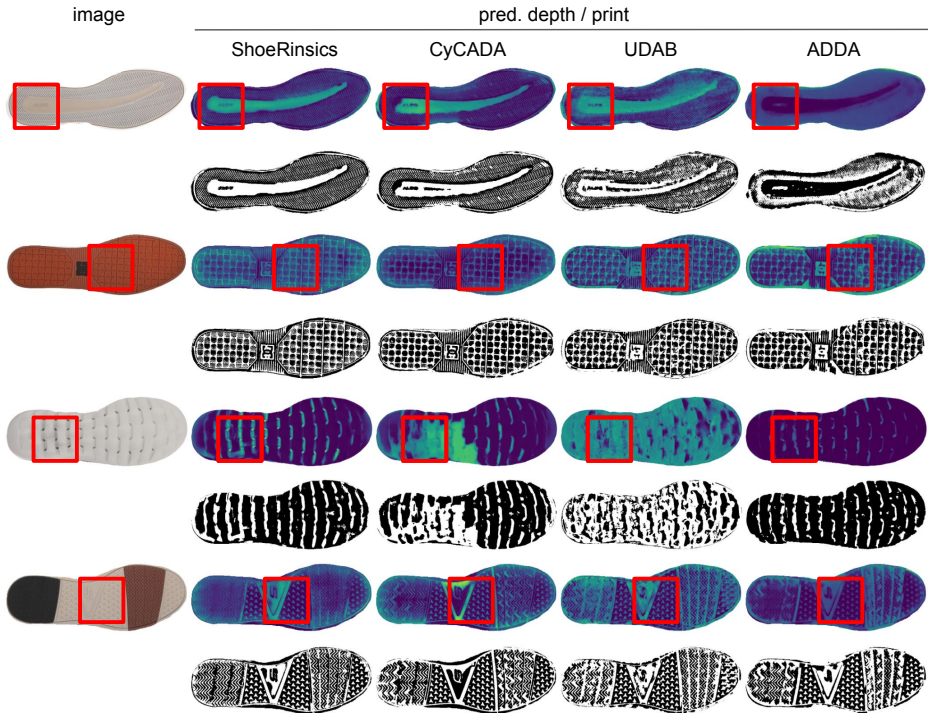


Fig. 10. Visual comparison on Real-test with depth predictors tailored from state-of-the-art domain adaptation methods [20,26,55]. *ShoeRinsics* works better than others on detail-rich regions.

10 Comparison with RIN

RIN [29] learns from unlabeled real images using intrinsic image decomposition. It breaks down images into albedo, normal and light. We integrate their normal predictions to obtain a depth prediction using the well-established Frankot Chellappa algorithm [16]. Thresholding this depth prediction gives us the shoeprint prediction which we compare to ground-truth shoeprint. In Figure 11, we compare the albedo, normal, depth and shoeprint predictions of RIN on Real-val with that of *ShoeRinsics*. We find that RIN performs very poorly on real shoes. Even though our focus is on the depth prediction, our albedo and normal predictions visually look better than the predictions made by RIN. More importantly, the poor normal predictions from RIN integrate to give low quality depth predictions and thus bad shoeprint predictions.

11 Implementation Details

Our decomposer (f_R) consists of a classic encoder-decoder structure with skip connections. We use separate decoders for albedo, normal, depth and light pre-

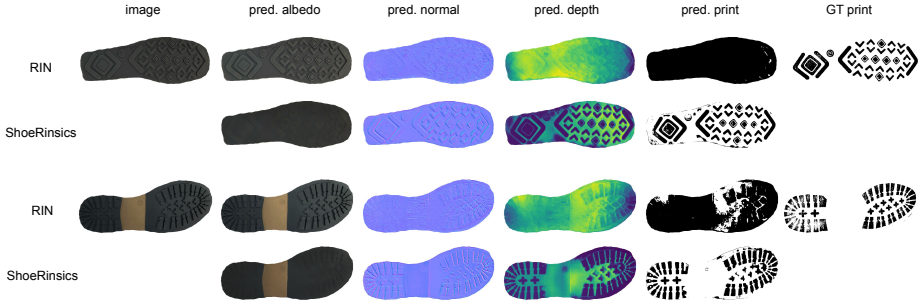


Fig. 11. Qualitative comparison between RIN [29] and *ShoeRinsics* on Real-val. Along with input images and ground-truth shoeprint, we show albedo, normal, depth, and print prediction. Note that RIN does not directly produce depth predictions. We obtain them by integrating their normal predictions using the well-established Frankot Chellappa algorithm [16]. As we can see, RIN produces poor quality albedo and normal predictions. The albedo predictions retain much of the shading information and the normal predictions are very noisy. The unsatisfactory normal predictions in RIN lead to bad depth and print predictions. Comparatively, *ShoeRinsics* is able to produce more likely albedo, normal, and depth predictions and thus predict shoeprints which are much closer to ground-truth.

dictions. All of the encoded input is passed to each of these decoders. The light decoder consists of residual blocks followed by a final convolution layer which outputs 17 numbers representing the probability of predicting the 17 light types in our synthetic training dataset. We use the output of the second last layer of the albedo, normal and depth decoder as the corresponding features. For light features, we use the 17 light probabilities.

The renderer (R) has a mirrored structure as the decomposer. R has separate encoders for albedo, depth, normal and light. The light encoder takes in a one-hot array representing the light configuration. The encoded information from each of the encoders is concatenated and passed to the decoder which predicts the synthetic or real image.

When passing decomposer outputs to the renderer in our main pipeline, we ensure that the decomposer outputs look similar to the synthetic albedo, depth, normal and light used to train the renderer. We set background (i.e., outside the shoe-sole) pixel values equal to 1 in the albedo, depth and normal predictions. We also use the Hard-Gumble trick to represent the light predictions as one-hot vectors instead of fractional probabilities for the renderer. This ensures that a path exists for gradient back-propagation through the light decoder while providing a one-hot representation of the light probabilities.

We use a ResNet backbone for the image translation generators ($G_{S \rightarrow R}$ and $G_{R \rightarrow S}$). The two generators have the exact same structure. They consist of 2 convolution layers with stride 2, followed by 9 residual blocks and finally 2 convolution layers coupled with nearest 2D upsampling layers with a scale factor of 2. The corresponding discriminators (D_R and D_S) are PatchGANs and consist

of 4 convolution layers with stride 2 followed by 2 convolution layers with stride 1. The convolution layers and residual blocks in the generators and discriminators are interspersed with batch normalization and the leakyReLU activation function.

The discriminator for feature alignment (D_{feat}) takes in the concatenation of the albedo, normal, and depth features as one input and the light features as a second input. These features are processed in two separate branches and the results are concatenated to produce the final output. Each of these branches consist of 3 convolution layers. The branch for the albedo, normal and depth features uses a kernel size of 3 (to encode some context) while the branch for light features use a kernel size of 1.

12 Pseudo Albedo Generation

We provide pseudo supervision on the albedo prediction on real images to guide intrinsic decomposition on real images. For this purpose, we first group the pixels in the real image using the mean-shift algorithm [18]. To generate the pseudo albedo labels, we work with the LAB color space since it is easier to distinguish hue (A and B) from brightness (L) in this color space. Additionally, to ensure that shading does not interfere with pixel grouping, we scale the L channel with a factor of 0.15. Note that ignoring L altogether would make it difficult to distinguish between black and white. It turns out that we do not need to work on full resolution images for pixel grouping. So, we first downsize our real-shoe images (from the original size of 389×864) to 67×150 for faster computation. After running mean-shift on the resulting shoe-sole pixels, we get an initial segmentation of the pixels in the real image. We define the color of each segment as the average color across that segment.

Next, we iteratively refine this initial segmentation for a maximum of 10 iterations. For each iteration we merge ‘nearby’ segments and update the color of the segments to reflect the segment updates. To merge segments, we find segments which are small in size and close to another segment both physically (share segment boundary) and numerically (have similar segment color). After merging the two segments, we update the color of the resulting segment as the average color across all the pixels in the new segment. We break the iterative refinement loop when we reach an iteration where the segmentation does not receive any updates or when the maximum iteration count (10) has been reached. Since this is a time-consuming process, we pre-determine the pseudo albedo for all real shoes and save them to be used directly during training.

13 Visualization of Synthetic Data

We visualize the different light environments in our synthetic dataset (Syn-train) in Figure 12. We have a total of 17 different light environments in our dataset. One of the light environment consists of diffuse white light. Eight light configurations consist of a light bulb providing directional light (from 8 different

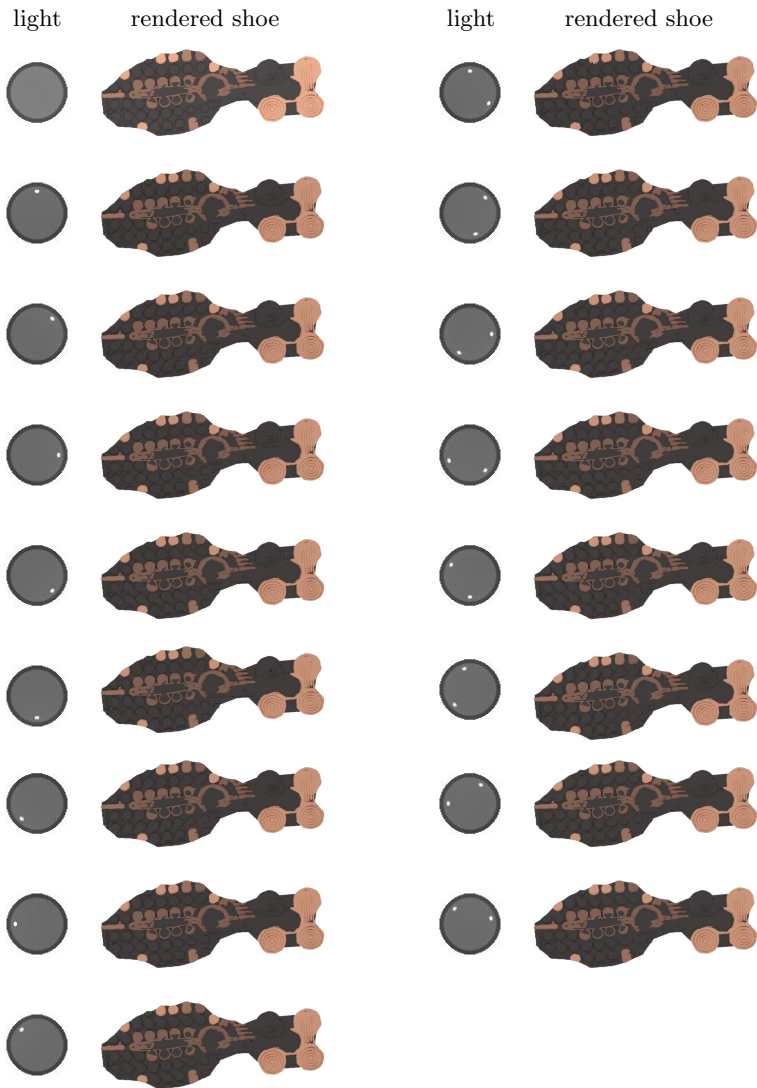


Fig. 12. Visualization of the 17 different light types in our synthetic dataset (Syn-train). We show a shiny sphere representing the light in the environment and a shoe rendered under that light condition. One light environment consists of diffuse white light. Eight light environments have a light bulb in addition to diffuse light to provide directional light. The other eight light environments consist of two light bulbs placed at 120° to each other in addition to diffuse white light.

directions) in addition to the diffuse white light. The other eight light configurations consists of two light bulbs at a 120° angle to each other in addition to the diffuse white light. For each light configuration, we visualize a shiny sphere in

place of the shoe to demonstrate the light placements. Additionally, we render an example synthetic shoe under all the different light conditions to show the effect of each of them.